Letter

Electrical activity of topological chiral edge magnons

Robin R. Neumann [1], Jürgen Henk [1], Ingrid Mertig [1], and Alexander Mook [2]
[1]*Institut für Physik, Martin-Luther-Universität Halle-Wittenberg, D-06099 Halle (Saale), Germany*
[2]*Institut für Physik, Johannes Gutenberg Universität Mainz, D-55128 Mainz, Germany*

(Received 20 December 2023; revised 8 March 2024; accepted 6 May 2024; published 24 May 2024)

Topological magnon insulators support chiral edge excitations, whose lack of electric charge makes them notoriously difficult to detect experimentally. We show that relativistic magnetoelectric coupling universally renders chiral edge magnons electrically active, thereby facilitating *electrical* probes of magnon topology. Considering a two-dimensional out-of-plane magnetized topological magnon insulator, we predict a fluctuation-activated electric polarization perpendicular to the sample edges. Furthermore, the chiral topological electromagnons give rise to a unique in-gap signal in electrical absorption experiments. These results suggest THz spectroscopy as a promising probe for topological magnons.

DOI: 10.1103/PhysRevB.109.L180412

Introduction. Topology has become a key concept in condensed matter physics, with the quantized Hall conductance being a prominent example [1,2]. Although topological band-structure theory can be carried over to magnons [3–8], i.e., the elementary excitations of magnetic order [9], their bosonic statistics does not give rise to quantized transport [10–17]. Furthermore, magnons lack electric charge, which, although being an attractive trait for technologies free of Joule heating [18], renders them "dark" in charge-probing spectroscopies. In addition, inelastic neutron scattering, which is the conventional probe of magnons, reveals their bulk band gaps, but fails to detect edge states [19,20]. In short, the state of the art does not offer an appropriate tool for the detection of topological magnons, and new ideas are needed [21–28].

Despite their charge neutrality, magnons can be manipulated by external electric fields, e.g., indirectly by magnetoelectrically controlling the ground state's spin texture [29,30]. Crucially, magnons also respond dynamically to electric fields. Those electrically active magnons, so-called *electromagnons*, have been studied by THz spectroscopy [31–36], by magnon-photon coupling in cavities [37–39], and by parametric amplification of topological magnons [22]. The experimental proof of principle for driving magnons electrically has already been provided [40].

Herein, we investigate the electrical activity of topological chiral edge magnons in ferromagnets in order to explore their spectroscopic signatures. Knowing that a flow of magnons induces electric fields [41,42] by virtue of the vacuum magnetoelectric (VME) effect [43–45], we first show that a flow of chiral edge magnons universally causes an electric edge polarization. Motivated by this result, we consider the Katsura-Nagaosa-Balatsky (KNB) mechanism [46] to study the electric polarization of a two-dimensional topological magnon insulator (TMI) and to disentangle contributions from topologically trivial and nontrivial magnons. Second, we investigate the response of topological magnons to external alternating electric fields in TMI nanoribbons and flakes, in which edge magnons cause electric absorption peaks within the magnon bulk band gap. Our results suggest that chiral edge magnons are electrically active and that terahertz spectroscopy could evidence their existence experimentally.

Edge-only approximation. We start with a simplified but instructive picture that is complemented in the next section. Magnons carry a magnetic moment $\boldsymbol{m}$, giving rise to a relativistic electric dipole $\boldsymbol{p} = \boldsymbol{v} \times \boldsymbol{m}/c^2$ ($\boldsymbol{v}$ magnon velocity, c speed of light), which is the VME effect resulting from Lorentz transformation from the magnon's rest frame to the laboratory frame [41,43–45]. For chiral edge magnons in two-dimensional and out-of-plane magnetized TMI, $\boldsymbol{m} \parallel \hat{\boldsymbol{z}}$ and

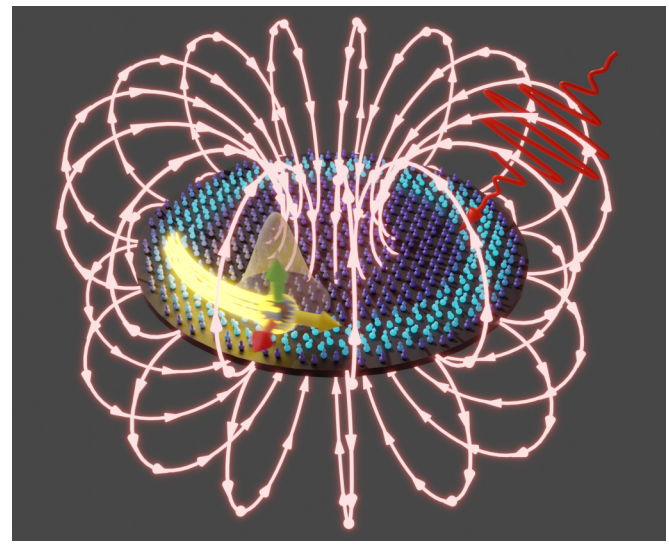

FIG. 1. Propagating chiral edge magnon in a disk-shaped topological magnon insulator. Arrows indicate velocity (yellow), magnetic dipole moment (green), and electric dipole moment (red, due to the vacuum magnetoelectric effect) of the wave packet (transparent sphere). The electric field (light red lines) follows from the generalized Biot-Savart law. The dark (light) blue arrows represent localized spins in their ground (excited) state. The red oscillating curve illustrates an external alternating electric field, which excites and probes chiral edge magnons.

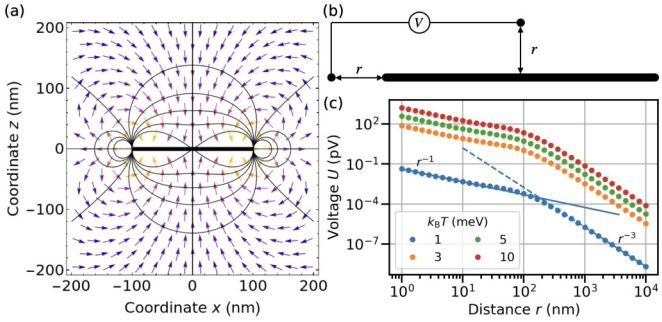

FIG. 2. Electric field of a magnetic disk in the xy plane and with a radius of 100 nm. (a) Field distribution in the xz plane ($y = 0$). Arrows and arrow colors indicate directions and magnitude of the electric field, respectively, while black lines indicate equipotential lines. The disk is indicated by the black rectangle at $z = 0$. (b) Schematic of a voltage measurement setup. (c) Estimated distance dependence of the voltage due to the vacuum magnetoelectric effect of topological magnons for the setup of panel (b). Dots represent numerical data, while straight and dashed lines are linear fits to $U(r)$ for $k_BT = 1$ meV (11.6 K). For parameters, see the text.

$\boldsymbol{p} \parallel \boldsymbol{v} \times \hat{\boldsymbol{z}}$ points along the local edge normal, as indicated in Fig. 1. The sign of $\boldsymbol{p}$ depends on the magnetization direction and on the velocity (hence, on the chirality) of the edge magnons. Since topological magnons do not exist in the magnetic ground state, finite temperatures are required. Although bulk magnons also exist at nonzero temperatures, they are neglected for now, since they are delocalized throughout the bulk and compensate each other's electric dipole moment. In contrast, the chiral edge magnons with opposite $\boldsymbol{p}$ are spatially separated, allowing for nonzero local electric fields.

The chiral magnon edge current causes an electric field $\boldsymbol{E} = -\nabla\phi$, whose scalar potential,

$$\phi(\boldsymbol{r}) = \frac{\mu_0 I_\mathrm{m}}{4\pi} \oint [\mathrm{d}\boldsymbol{r}' \times \hat{\boldsymbol{m}}(\boldsymbol{r}')] \cdot \frac{\boldsymbol{r} - \boldsymbol{r}'}{|\boldsymbol{r} - \boldsymbol{r}'|^3}, \tag{1}$$

is obtained from a generalized Biot-Savart law [41,42] (μ_0 is the vacuum permeability, I_m is the magnetization current, and $\hat{\boldsymbol{m}}$ is the direction of the magnetic dipole).

For a magnetic current carried by chiral magnons on a circular trajectory of radius R, we write $\boldsymbol{r} = \rho\hat{\boldsymbol{e}}_\rho(\varphi) + z\hat{\boldsymbol{e}}_z$ in cylindrical coordinates; $\hat{\boldsymbol{e}}_z$ ($\hat{\boldsymbol{e}}_\rho$) is out-of-plane (radial) to the magnetic current loop. If $R \ll \rho$, we approximate

$$\phi(\rho, \varphi, z) \approx \frac{\mu_0 I_\mathrm{m}}{4} \frac{R^2(\rho^2 - 2z^2)}{(\rho^2 + z^2)^{5/2}}, \tag{2}$$

while for $\rho = 0$ the exact potential reads

$$\phi(0, \varphi, z) = -\frac{\mu_0 I_\mathrm{m}}{2} \frac{R^2}{(R^2 + z^2)^{3/2}} \tag{3}$$

[see the Supplemental Material (SM) [47]]. Thus, the potential drops with distance as z^{-3} in the far-field limit. The sign of I_m, i.e., the chirality of the edge magnons, determines the direction of the electric field $\boldsymbol{E}$. As expected, the $\boldsymbol{E}$ field lines point radially outward from the edge of the disk and resemble a dipole field close to the edge [see Fig. 2(a)]. The largest electric field is found in the vicinity of the edges hosting the chiral edge magnons.

To estimate $\boldsymbol{E}$, we compute $I_\mathrm{m} = \frac{g\mu_B v}{2\pi} \int_{-\pi/a}^{\pi/a} \mathrm{d}k\rho(\varepsilon_k)$ (g is the Landé g-factor, μ_B is the Bohr magneton, a is the lattice constant, and v is the edge magnon's group velocity). The occupation is given by $\rho(\varepsilon) = [\exp(\varepsilon/(k_BT)) - 1]^{-1}$ (k_B is the Boltzmann constant, and T is the temperature). We assume $a = 1$ nm and, in order to describe van-der-Waals magnets [20,48], $v = 1000\,\mathrm{ms}^{-1}$, $\varepsilon_k = \hbar v k + 12$ meV (i.e., the topological band gap is 4 meV). The voltage $U(r) = \phi(r, 0, 0) - \phi(0, 0, r)$ between two leads at a distance r from the edge and the center of the disk is evaluated numerically [Fig. 2(b)]. Its r-dependence, shown in Fig. 2(c) for selected temperatures, exhibits two regimes: $r \ll R$ with an r^{-1}-dependence, and $r \gg R$ with an r^{-3}-dependence. The crossover is around $R = 100$ nm. These results suggest that a nanovolt-sensitive measurement could prove the existence of chiral edge magnons. We now contrast the edge-only approximation (EOA) with a microscopic theory that takes into account all magnon modes.

Microscopic theory. We consider a two-dimensional TMI on a honeycomb lattice, which is an effective model for van-der-Waals magnets. The Hamiltonian

$$\mathcal{H} = -\sum_{r=1}^{3} \frac{J_r}{2\hbar^2} \sum_{\langle ij\rangle_r} \boldsymbol{S}_i \cdot \boldsymbol{S}_j + \frac{1}{2\hbar^2} \sum_{\langle ij\rangle_2} \boldsymbol{D}_{ij} \cdot (\boldsymbol{S}_i \times \boldsymbol{S}_j) - \frac{A}{\hbar^2} \sum_i \left(S_i^z\right)^2 \tag{4}$$

includes Heisenberg exchange interactions J_r up to third nearest neighbors, out-of-plane Dzyaloshinskii-Moriya interaction (DMI) $\boldsymbol{D}_{ij} = \pm D_z\hat{\boldsymbol{z}}$ between second nearest neighbors, and out-of-plane anisotropy A ($\hbar$ is the reduced Planck constant). In the following, we choose relative parameters: $J_1 = 1, J_2 = 0.25, J_3 = 0, D_z = -0.1, A = 0.1$, and $S = 1$. The ground state is an out-of-plane collinear ferromagnet.

The model (4) is known to yield topological magnons in linear spin-wave theory [7,8], which are shown for the armchair nanoribbon geometry in Fig. 3(b). We present the linear spin wave theory and discuss its validity in the present context in the SM [47]. The in-gap states have positive (negative) group velocity and are localized on the left (right) edge. The relation between velocity and localization depends on the Chern number, which can be reversed with the magnetization or the sign of D_z.

Assuming a topologically trivial electronic band gap, the charge dynamics of the electrons on the energy scale of the magnetic interactions far below the electronic gap of a Mott insulator is governed by the magnetoelectric coupling [49]. The relativistic electric dipole between two spins at sites i and j reads $\boldsymbol{p}_{ij} = q_{ij}\boldsymbol{e}_{ij} \times (\boldsymbol{S}_i \times \boldsymbol{S}_j)/\hbar^2$ according to the spin-current [or Katsura-Nagaosa-Balatsky (KNB)] mechanism [46,50] (q_{ij} is the effective charge, $\boldsymbol{e}_{ij}$ is the bond vector from site i to site j, and $\boldsymbol{S}_i$ and $\boldsymbol{S}_j$ are spin operators). As shown in the SM [47], the VME and the KNB effects are equivalent for magnons in Heisenberg ferromagnets, but the KNB effect can be larger by five to six orders of magnitude. In the following, we study the implications of the KNB effect for topological magnons.

We expand $\boldsymbol{p}_{ij} = \boldsymbol{p}_{ij}^{(0)} + \boldsymbol{p}_{ij}^{(1)} + \boldsymbol{p}_{ij}^{(2)} + \cdots$ by means of the Holstein-Primakoff transformation [51], where the superscript denotes the number of bosons (explicit expressions for the

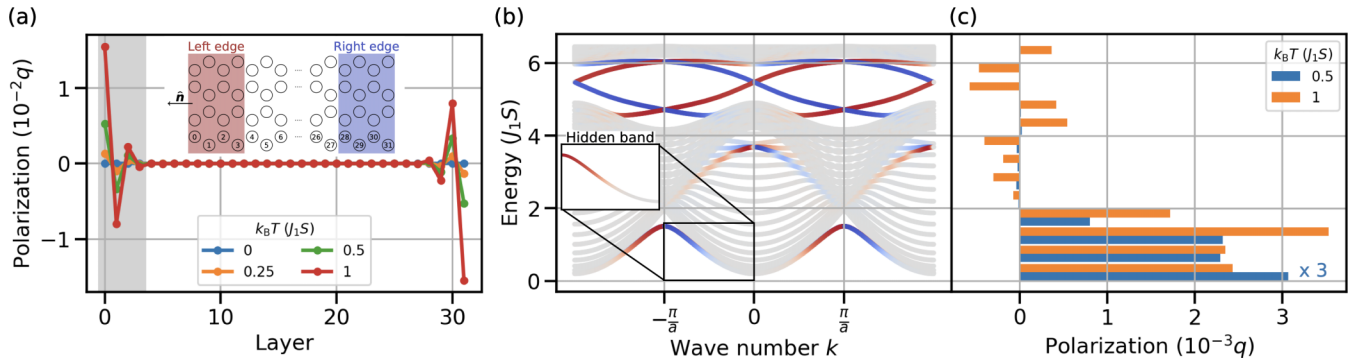

FIG. 3. Electric polarization and magnons of a nanoribbon in armchair nanoribbon geometry with 32 layers. (a) Layer-resolved electric polarization due to the Katsura-Nagaosa-Balatsky effect for various temperatures (as indicated) projected onto the outward-facing in-plane normal vector $\hat{\boldsymbol{n}}$ of the left edge. Inset: section of the nanoribbon including layer labels and the normal vector $\hat{\boldsymbol{n}}$. The system is finite (infinite) along the horizontal (vertical) direction. (b) Magnon spectrum. Probability amplitudes of the left (red) and right (blue) edge [defined as the four outermost layers at each edge side; cf. the inset in panel (a)] are encoded by color. Inset: hidden band covered by the lowest band. (c) Energy-resolved contributions of the magnons to the electric polarization at the left edge [highlighted in panel (a) by a gray background] for two selected temperatures (as indicated). Each bar comprises contributions accumulated in an energy interval of $J_1S/2$. The blue bars are multiplied by 3 for better visibility. Parameters read $J_1 = 1, J_2 = 0.25, J_3 = 0, D_z = -0.1, A = 0.1$, and $S = 1$. Results for other terminations can be found in the SM [47].

operators are provided in the SM [47]). $\boldsymbol{p}_{ij}^{(0)}$ is the classical ground-state polarization, which is zero in our case. The expectation value of $\boldsymbol{p}_{ij}^{(1)}$ vanishes in equilibrium, but encodes the dynamic electric dipole moment associated with spin dynamics, and the bilinear $\boldsymbol{p}_{ij}^{(2)}$ tells about the expectation value per magnon. In equilibrium, the fluctuation-induced $\boldsymbol{p}_{ij}^{(2)}$ is the dominant contribution to the macroscopic polarization.

Below, we consider the layer-resolved polarization,

$$\boldsymbol{P}_n = \frac{q}{\hbar^2 L} \sum_{\substack{\langle ij \rangle \\ i \in L_n}} \boldsymbol{e}_{ij} \times (\boldsymbol{S}_i \times \boldsymbol{S}_j), \tag{5}$$

for all layers n in the nanoribbon, which is a sum over all intersite electric dipole moments $\boldsymbol{p}_{ij}$ in that layer (L_n is the set of all sites in layer n, and L is the circumference of the nanoribbon). The thermal equilibrium expectation value of $\boldsymbol{P}_n$ (originating from $\boldsymbol{p}_{ij}^{(2)}$) projected onto the in-plane normal vector $\hat{\boldsymbol{n}}$ of the left edge, shown in Fig. 3(a), features nonzero values at the edges of the nanoribbon, while it vanishes in the bulk. Inversion symmetry dictates that the polarizations at opposite edges are antiparallelly oriented. However, in the EOA based on the VME effect and the chirality of the edge magnons [cf. Fig. 3(b)], one would expect a *negative* projected polarization at the left edge, which is opposite to the numerical results.

This discrepancy is understood by analyzing the energy-resolved contributions to the left-edge polarization $\sum_{n=0}^{3} \boldsymbol{P}_n$ [see Fig. 3(c); layers 0–3 are highlighted in Fig. 3(a)]. There exist not only contributions from within the topological band gap, but also much larger ones from energies below the gap. The latter arise from trivial subgap edge modes [see Fig. 3(b)], whose thermal occupation is larger than that of the nontrivial in-gap states. The existence of trivial subgap edge modes is unavoidable: these arise from the weaker effective internal magnetic field for spins at the edges (missing neighbor sites). The subgap states highlighted in the inset of Fig. 3(b) (these are hidden below the lowest band) have a velocity opposite to that of the nontrivial mode localized at the same edge, and therefore an opposite electric dipole moment. The contributions of trivial subgap modes to $\sum_{n=0}^{3} \boldsymbol{P}_n$ dominate over those of the nontrivial in-gap modes at all temperatures. Furthermore, the trivial contributions proved robust against disorder and manipulations of the edges (see the SM [47]).

In short, the equilibrium properties of the topological magnons are overshadowed by those of trivial magnons, and our microscopic theory deems the EOA incomplete. Furthermore, the edge polarization may include a ground-state contribution that results from spin canting induced by stray fields.

Absorption of alternating electric fields. The above discussion demonstrates the need to go beyond thermal equilibrium, in which subgap states are favored over in-gap states. As we show in the SM [47], the in-gap states do not respond to alternating magnetic fields. Therefore, we study the possibility to address resonantly the magnons with alternating *electric* fields $\boldsymbol{E}(t)$ by including a perturbation

$$\mathcal{H}' = -V\boldsymbol{P} \cdot \boldsymbol{E}(t) = \frac{q}{\hbar^2} \sum_{\langle ij \rangle} (\boldsymbol{e}_{ij} \times \boldsymbol{E}(t)) \cdot (\boldsymbol{S}_i \times \boldsymbol{S}_j) \tag{6}$$

to the Hamiltonian (4) ($\boldsymbol{P}$ is the total electric polarization). This form suggests that the external electric field induces a time-varying DMI, the corresponding DMI vector of which is out-of-plane (in-plane) for in-plane (out-of-plane) fields.

The linear response of $\boldsymbol{P}$ to the perturbation, $\Delta\langle P_\mu(\omega)\rangle = \chi_{\mu\nu}(\omega) E_\nu(\omega)$, is quantified by the electric susceptibility $\chi_{\mu\nu}(\omega)$ ($\mu, \nu = x, y, z$; implicit summation over ν). In Kubo's formalism [52,53], $\chi_{\mu\nu}(\omega) = -VC^{\mathrm{R}}_{P_\mu P_\nu}(\omega)$ is obtained from the retarded polarization autocorrelation function $C^{\mathrm{R}}_{P_\mu P_\nu}(\omega)$, which is evaluated in the SM [47]. There are various types of contributions $\chi^{(i)}_{\mu\nu}$ to $\chi_{\mu\nu}$, among them one- ($i = 1$; leading order derived from $\boldsymbol{p}_{ij}^{(1)}$) and two-magnon processes ($i = 2$; leading order derived from $\boldsymbol{p}_{ij}^{(2)}$). While the one-magnon processes are governed by the (out-of-plane or transversal)

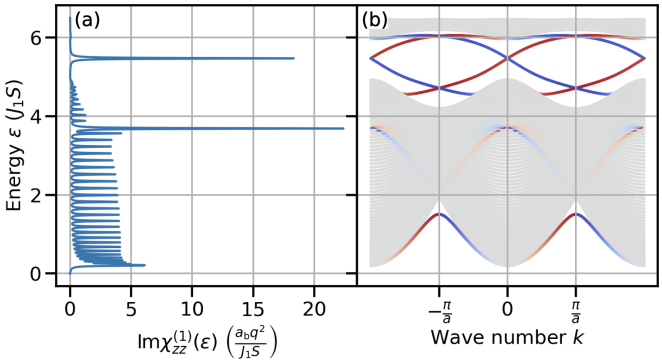

FIG. 4. Electric susceptibility of a 120-layers-wide nanoribbon with armchair terminations. (a) Imaginary part of the one-magnon susceptibility vs energy. (b) Magnon spectrum with localization at the left (red) and right (blue) edge encoded by color. a_b is the bulk lattice constant of the underlying honeycomb lattice, while $a = \sqrt{3}a_b$ is the lattice constant of the nanoribbon. The width of the Lorentzians is $\eta = 0.01J_1S$. Parameters as for Fig. 3. Results for other terminations can be found in the SM [47].

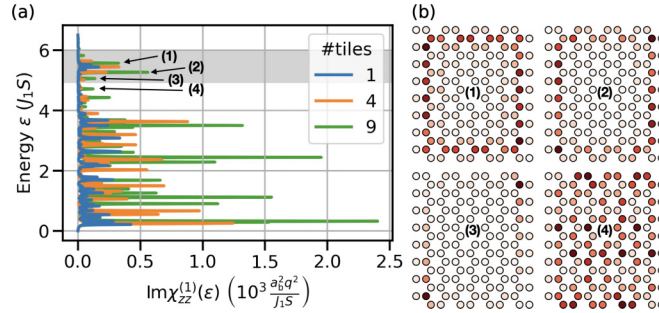

FIG. 5. Electric susceptibility of a flake of 1152 spins cut into four (nine) smaller equally sized tiles [see the legend in panel (a)]. (a) Energy-resolved imaginary part of the electric one-magnon susceptibility. For the nine-tile spectrum (green line), selected in-gap resonances **(1)**–**(4)** are marked with arrows. The gray background indicates the topological bulk band gap. (b) Real-space probability distributions of the four electrically active magnon modes **(1)**–**(4)** marked in panel (a), one tile for each mode (as indicated). Nine of these tiles make up the green absorption spectrum in panel (a). The width of the Lorentzians is $\eta = 0.01J_1S$. Parameters as for Fig. 3.

fluctuations of the magnons' electric dipole moments about their mean value, the two-magnon processes are governed by the bilinear part of the total dipole moment that is also responsible for the finite mean value in equilibrium (longitudinal fluctuations). Therefore, one-magnon processes appear for out-of-plane electric fields, while two-magnon processes appear for in-plane electric fields. Since according to Eq. (6) only the former induces in-plane DMI, which breaks magnon-number conservation, only one-magnon processes may change the magnon number, while two-magnon processes can only cause interband transitions of thermally excited magnons. Thus, contrary to $\chi^{(1)}_{\mu\nu}$, $\chi^{(2)}_{\mu\nu}$ can be frozen out. We therefore focus on one-magnon processes in the rest of the paper, while delegating further details, mathematical expressions, derivations, and results for two-magnon processes to the SM [47].

The imaginary part

$$\mathrm{Im}\chi^{(1)}_{\mu\mu}(\omega) = \pi V \sum_{n=1}^{N} \left|\left(\mathcal{P}^{(1)}_{\mu}\right)_n\right|^2 \delta(\hbar\omega - \varepsilon_{n,\boldsymbol{k}=\boldsymbol{0}}) \qquad (7)$$

of the diagonal electric one-magnon susceptibility ($\omega > 0$, N is the number of bands) contains the linear electric dipole element $(\mathcal{P}^{(1)}_{\mu})_n$ for component μ and band n, whose general expression is derived in the SM [47]. The δ-distribution, which we replace by a Lorentzian of width η for numerical calculations, ensures energy conservation, such that resonance frequencies appear at the eigenfrequencies of the system, while only magnons at $\boldsymbol{k} = \boldsymbol{0}$ can be probed due to momentum conservation.

Returning to the honeycomb model, absorption appears only for $\mu = z$: it shows a pronounced in-gap peak just below $\varepsilon/(J_1S) = 6$, which is attributed to topological magnons (see Fig. 4). In the SM [47], we show that *the absorption only takes place at the edges*, therefore, only modes with nonzero probability amplitude at the edges may contribute. Bulk modes have nonzero probability amplitudes at the edges as well, but cause peaks above and below the gap.

Together with inelastic neutron scattering, which can locate gaps in the bulk magnon spectrum, in-gap peaks of $\mathrm{Im}\chi^{(1)}_{zz}(\omega)$ could enable the detection of topological magnons in principle. Momentum conservation tells that only topological magnons with $\boldsymbol{k} = \boldsymbol{0}$ contribute to the signal; however, it is not guaranteed that topological magnons exist at this particular $\boldsymbol{k}$ (see the SM for a counterexample [47]). Thus, in-gap peaks are not a necessary consequence of topological edge modes. Furthermore, absorption at a sample's edge could be overshadowed by other sources and hence might be hard to resolve in experiment.

The above suggests that momentum conservation has to be lifted. We therefore consider the electric absorption of flakes instead of nanoribbons. While a large flake is roughly similar to a nanoribbon, increasing deviations are expected upon shrinking the flake. We have computed the electric one-magnon absorption of a flake encompassing 1152 spins [blue line in Fig. 5(a)] that is "cut" into four (orange line) and nine equally sized smaller tiles (green line). This cutting increases the signal magnitude of infinite-wavelength peaks due to the introduction of internal edges and leads to additional peaks from in-gap states with smaller wavelengths.

To prove the topological origin of the in-gap peaks for the green line, we have selected four peaks [labeled **(1)**–**(4)** in Fig. 5(a)], for which the real-space probability distribution of the corresponding magnon states is shown in Fig. 5(b). Each flake depicts one of the nine tiles responsible for the green absorption spectrum in Fig. 5(a). The darker the color, the stronger the localization of the corresponding magnon mode at that site. In the cases **(1)**, **(2)**, and **(3)**, the electrically active modes have vanishing weights in the bulk. In contrast, mode **(4)** is delocalized throughout the bulk. The topological bulk gap, indicated by a horizontal gray stripe in the background of Fig. 5(a), includes modes **(1)**–**(3)**, while **(4)** falls outside this energy window, demonstrating the topological origin of the *in-gap* absorption peaks.

Quantitative estimate. The effective charge is estimated as $q \approx 10^{-4}|e|$ to $10^{-3}|e|$ for GaV_4S_8 [54], $CrBr_3$ [55], and YIG [56] (cf. the SM [47]; $|e|$ is the elementary charge).

Here, we present calculations based on Heisenberg-DMI and Heisenberg-Kitaev models for the experimental parameters of CrI_3 [57] (cf. the SM [47]), a putative TMI. The three-dimensional electric edge polarization, which depends on the weight of the edges in the probed volume, is estimated to about $10\,\mu C/m^2$ within the first four layers. For the imaginary part of the three-dimensional electric susceptibility, which is inversely proportional to the linewidth η, we obtain $6\times10^{-3}\varepsilon_0$ for $\eta = 0.1$ meV (ε_0 is the vacuum permittivity). This value decreases with increasing size of the nanoribbon, as is expected for edge effects. We expect that our prediction qualitatively applies as well to other ferromagnetic TMI, such as $Lu_2V_2O_7$ [12], Cu(1,3-benzenedicarboxylate) [14,19], $CrSiTe_3$ and $CrGeTe_3$ [20], and VI_3 [58], all of which have electronic band gaps much larger than the magnon bandwidth [19,20,48,59–66].

Discussion. We have investigated the electric properties of topological chiral edge magnons in equilibrium and nonequilibrium. In the edge-only approximation, topological magnons give rise to an electric edge polarization by thermal fluctuations even in centrosymmetric systems. However, the model calculations based on the KNB effect identified further contributions by trivial edge modes, which dominate the overall signal. Nonetheless, by addressing the topological magnons directly with alternating electric fields of corresponding frequencies, we demonstrated that these modes may be electrically active, as is indicated by peaks in the one-magnon electric susceptibility. These topological electromagnons have infinite wavelengths and, depending on their specific dispersion relation, might not be present in every nanoribbon. The electric absorption by topological edge magnons in flakes can be tuned by the edge-to-area ratio so that additional peaks from magnons with a finite wavelength appear, and the signal of magnons with infinite wavelength is increased. Hence, we believe that THz spectroscopy can be regarded a probe for topological magnons.

Future research in "topological electromagnonics" could be directed at a *local* THz probe of chiral edge states, as provided by scattering-type scanning near-field optical microscopy [67–70], at a topological electromagnon-polariton formation in THz cavities [38], and at the existence of topological electromagnons beyond the relativistic KNB mechanism [50]. We hope that our results provide an additional impetus to search for candidate materials with nontrivial magnon band structures and strong magnetoelectric coupling, and to explore the relation of electromagnons to magnon orbitronics [71,72].

Acknowledgments. This work was funded by the Deutsche Forschungsgemeinschaft (DFG, German Research Foundation)–Project-ID 328545488–TRR 227, Project No. B04; and Project No. 504261060 (Emmy Noether Programme).

[1] K. v. Klitzing, G. Dorda, and M. Pepper, New method for high-accuracy determination of the fine-structure constant based on quantized Hall resistance, Phys. Rev. Lett. **45**, 494 (1980).

[2] F. D. M. Haldane, Model for a quantum Hall effect without landau levels: Condensed-matter realization of the "parity anomaly," Phys. Rev. Lett. **61**, 2015 (1988).

[3] R. Matsumoto and S. Murakami, Theoretical prediction of a rotating magnon wave packet in ferromagnets, Phys. Rev. Lett. **106**, 197202 (2011).

[4] L. Zhang, J. Ren, J.-S. Wang, and B. Li, Topological magnon insulator in insulating ferromagnet, Phys. Rev. B **87**, 144101 (2013).

[5] R. Shindou, R. Matsumoto, S. Murakami, and J.-I. Ohe, Topological chiral magnonic edge mode in a magnonic crystal, Phys. Rev. B **87**, 174427 (2013).

[6] A. Mook, J. Henk, and I. Mertig, Edge states in topological magnon insulators, Phys. Rev. B **90**, 024412 (2014).

[7] S. A. Owerre, A first theoretical realization of honeycomb topological magnon insulator, J. Phys.: Condens. Matter **28**, 386001 (2016).

[8] S. K. Kim, H. Ochoa, R. Zarzuela, and Y. Tserkovnyak, Realization of the haldane-kane-mele model in a system of localized spins, Phys. Rev. Lett. **117**, 227201 (2016).

[9] F. Bloch, Zur Theorie des Ferromagnetismus, Z. Phys. **61**, 206 (1930).

[10] R. Tao and K. Maki, Quantum Hall effect of two-dimensional interacting boson systems, Phys. Lett. A **116**, 277 (1986).

[11] H. Katsura, N. Nagaosa, and P. A. Lee, Theory of the thermal Hall effect in quantum magnets, Phys. Rev. Lett. **104**, 066403 (2010).

[12] Y. Onose, T. Ideue, H. Katsura, Y. Shiomi, N. Nagaosa, and Y. Tokura, Observation of the Magnon Hall effect, Science **329**, 297 (2010).

[13] R. Matsumoto, R. Shindou, and S. Murakami, Thermal Hall effect of magnons in magnets with dipolar interaction, Phys. Rev. B **89**, 054420 (2014).

[14] M. Hirschberger, R. Chisnell, Y. S. Lee, and N. P. Ong, Thermal Hall effect of spin excitations in a Kagome Magnet, Phys. Rev. Lett. **115**, 106603 (2015).

[15] K. Nakata, J. Klinovaja, and D. Loss, Magnonic quantum Hall effect and Wiedemann-Franz law, Phys. Rev. B **95**, 125429 (2017).

[16] A. Mook, B. Göbel, J. Henk, and I. Mertig, Taking an electron-magnon duality shortcut from electron to magnon transport, Phys. Rev. B **97**, 140401(R) (2018).

[17] R. R. Neumann, A. Mook, J. Henk, and I. Mertig, Thermal Hall effect of magnons in collinear antiferromagnetic insulators: Signatures of magnetic and topological phase transitions, Phys. Rev. Lett. **128**, 117201 (2022).

[18] A. V. Chumak, V. I. Vasyuchka, A. A. Serga, and B. Hillebrands, Magnon spintronics, Nat. Phys. **11**, 453 (2015).

[19] R. Chisnell, J. S. Helton, D. E. Freedman, D. K. Singh, R. I. Bewley, D. G. Nocera, and Y. S. Lee, Topological magnon bands in a kagome lattice ferromagnet, Phys. Rev. Lett. **115**, 147201 (2015).

[20] F. Zhu, L. Zhang, X. Wang, F. J. dos Santos, J. Song, T. Mueller, K. Schmalzl, W. F. Schmidt, A. Ivanov, J. T. Park, J. Xu, J. Ma, S. Lounis, S. Blügel, Y. Mokrousov, Y. Su, and T. Brückel, Topological magnon insulators in two-dimensional van der Waals ferromagnets $CrSiTe_3$ and $CrGeTe_3$: Toward intrinsic gap-tunability, Sci. Adv. **7**, eabi7532 (2021).

[21] B. Perreault, J. Knolle, N. B. Perkins, and F. J. Burnell, Raman scattering in correlated thin films as a probe of chargeless surface states, Phys. Rev. B **94**, 060408(R) (2016).

[22] D. Malz, J. Knolle, and A. Nunnenkamp, Topological magnon amplification, Nat. Commun. **10**, 3937 (2019).

[23] J. Feldmeier, W. Natori, M. Knap, and J. Knolle, Local probes for charge-neutral edge states in two-dimensional quantum magnets, Phys. Rev. B **102**, 134423 (2020).

[24] A. Rustagi, I. Bertelli, T. van der Sar, and P. Upadhyaya, Sensing chiral magnetic noise via quantum impurity relaxometry, Phys. Rev. B **102**, 220403(R) (2020).

[25] V. Guemard and A. Manchon, Unified formulation of interfacial magnonic pumping from noncollinear magnets, Phys. Rev. B **105**, 054433 (2022).

[26] B. Hetényi, A. Mook, J. Klinovaja, and D. Loss, Long-distance coupling of spin qubits via topological magnons, Phys. Rev. B **106**, 235409 (2022).

[27] A. Mitra, A. Corticelli, P. Ribeiro, and P. A. McClarty, Magnon interference tunneling spectroscopy as a probe of 2D magnetism, Phys. Rev. Lett. **130**, 066701 (2023).

[28] E. Viñas Boström, T. S. Parvini, J. W. McIver, A. Rubio, S. V. Kusminskiy, and M. A. Sentef, Direct optical probe of magnon topology in two-dimensional quantum magnets, Phys. Rev. Lett. **130**, 026701 (2023).

[29] C. Liu, Y. Luo, D. Hong, S. S.-L. Zhang, H. Saglam, Y. Li, Y. Lin, B. Fisher, J. E. Pearson, J. S. Jiang, H. Zhou, J. Wen, A. Hoffmann, and A. Bhattacharya, Electric field control of magnon spin currents in an antiferromagnetic insulator, Sci. Adv. **7**, eabg1669 (2021).

[30] F. Li, Y. Guan, P. Wang, Z. Wang, C. Fang, K. Gu, and S. S. P. Parkin, All-electrical reading and writing of spin chirality, Sci. Adv. **8**, eadd6984 (2022).

[31] T. Moriya, Far infrared absorption by two magnon excitations in aniferromagnets, J. Phys. Soc. Jpn. **21**, 926 (1966).

[32] T. Moriya, Theory of absorption and scattering of light by magnetic crystals, J. Appl. Phys. **39**, 1042 (1968).

[33] T. Moriya, Light scattering by two-magnon excitations in ferromagnets, Prog. Theor. Phys. Suppl. **46**, 121 (1970).

[34] A. Pimenov, A. A. Mukhin, V. Y. Ivanov, V. D. Travkin, A. M. Balbashov, and A. Loidl, Possible evidence for electromagnons in multiferroic manganites, Nat. Phys. **2**, 97 (2006).

[35] A. Pimenov, A. Loidl, A. A. Mukhin, V. D. Travkin, V. Yu. Ivanov, and A. M. Balbashov, Terahertz spectroscopy of electromagnons in $Eu_{1-x}Y_xMnO_3$, Phys. Rev. B **77**, 014438 (2008).

[36] N. Kida, Y. Ikebe, Y. Takahashi, J. P. He, Y. Kaneko, Y. Yamasaki, R. Shimano, T. Arima, N. Nagaosa, and Y. Tokura, Electrically driven spin excitation in the ferroelectric magnet $DyMnO_3$, Phys. Rev. B **78**, 104414 (2008).

[37] T. Hirosawa, A. Mook, J. Klinovaja, and D. Loss, Magnetoelectric cavity magnonics in skyrmion crystals, PRX Quantum **3**, 040321 (2022).

[38] J. B. Curtis, A. Grankin, N. R. Poniatowski, V. M. Galitski, P. Narang, and E. Demler, Cavity magnon-polaritons in cuprate parent compounds, Phys. Rev. Res. **4**, 013101 (2022).

[39] Z. Toklikishvili, L. Chotorlishvili, R. Khomeriki, V. Jandieri, and J. Berakdar, Electrically controlled entanglement of cavity photons with electromagnons, Phys. Rev. B **107**, 115126 (2023).

[40] T. Kubacka, J. A. Johnson, M. C. Hoffmann, C. Vicario, S. de Jong, P. Beaud, S. Grübel, S.-W. Huang, L. Huber, L. Patthey, Y.-D. Chuang, J. J. Turner, G. L. Dakovski, W.-S. Lee, M. P. Minitti, W. Schlotter, R. G. Moore, C. P. Hauri, S. M. Koohpayeh, V. Scagnoli *et al.*, Large-amplitude spin dynamics driven by a THz pulse in resonance with an electromagnon, Science **343**, 1333 (2014).

[41] F. Meier and D. Loss, Magnetization transport and quantized spin conductance, Phys. Rev. Lett. **90**, 167204 (2003).

[42] F. Schütz, M. Kollar, and P. Kopietz, Persistent spin currents in mesoscopic Heisenberg rings, Phys. Rev. Lett. **91**, 017205 (2003).

[43] J. E. Hirsch, Overlooked contribution to the Hall effect in ferromagnetic metals, Phys. Rev. B **60**, 14787 (1999).

[44] V. Hnizdo, Magnetic dipole moment of a moving electric dipole, Am. J. Phys. **80**, 645 (2012).

[45] D. J. Griffiths and V. Hnizdo, Mansuripur's paradox, Am. J. Phys. **81**, 570 (2013).

[46] H. Katsura, N. Nagaosa, and A. V. Balatsky, Spin current and magnetoelectric effect in noncollinear magnets, Phys. Rev. Lett. **95**, 057205 (2005).

[47] See Supplemental Material at http://link.aps.org/supplemental/10.1103/PhysRevB.109.L180412 for details about the solution of the Biot-Savart law, linear spin wave theory, magnon expansion of total and local electric polarization operators, estimation of the effective charge, comparison between the VME and KNB mechanisms, derivation for the electric and magnetic susceptibilities, as well as additional results for the electric polarization and electric and magnetic susceptibilities for Heisenberg-DMI and Heisenberg-Kitaev models. Moreover, the influence of increased easy-axis anisotropies at the edges and on-site disorder on the local electric polarization is studied. The Supplemental Material cites Refs. [7,8,41,42,46,52–57,73–92].

[48] L. Chen, J.-H. Chung, M. B. Stone, A. I. Kolesnikov, B. Winn, V. O. Garlea, D. L. Abernathy, B. Gao, M. Augustin, E. J. G. Santos, and P. Dai, Magnetic field effect on topological spin excitations in CrI_3, Phys. Rev. X **11**, 031047 (2021).

[49] A. Bolens, Theory of electronic magnetoelectric coupling in d^5 Mott insulators, Phys. Rev. B **98**, 125135 (2018).

[50] Y. Tokura, S. Seki, and N. Nagaosa, Multiferroics of spin origin, Rep. Prog. Phys. **77**, 076501 (2014).

[51] T. Holstein and H. Primakoff, Field dependence of the intrinsic domain magnetization of a ferromagnet, Phys. Rev. **58**, 1098 (1940).

[52] R. Kubo, Statistical-mechanical theory of irreversible processes. I. General theory and simple applications to magnetic and conduction problems, J. Phys. Soc. Jpn. **12**, 570 (1957).

[53] H. Bruus and K. Flensberg, *Many-Body Quantum Theory in Condensed Matter Physics: An Introduction* (Oxford University Press, Oxford, 2004).

[54] S. A. Nikolaev and I. V. Solovyev, Microscopic theory of electric polarization induced by skyrmionic order in GaV_4S_8, Phys. Rev. B **99**, 100401(R) (2019).

[55] A. O. Fumega and J. L. Lado, Moiré-driven multiferroic order in twisted $CrCl_3$, $CrBr_3$ and CrI_3 bilayers, 2D Mater. **10**, 025026 (2023).

[56] T. Liu and G. Vignale, Electric control of spin currents and spin-wave logic, Phys. Rev. Lett. **106**, 247203 (2011).

[57] L. Chen, J.-H. Chung, B. Gao, T. Chen, M. B. Stone, A. I. Kolesnikov, Q. Huang, and P. Dai, Topological spin excitations in honeycomb ferromagnet CrI_3, Phys. Rev. X **8**, 041028 (2018).

[58] H. Zhang, C. Xu, C. Carnahan, M. Sretenovic, N. Suri, D. Xiao, and X. Ke, Anomalous thermal Hall effect in an insulating van der Waals magnet, Phys. Rev. Lett. **127**, 247202 (2021).

[59] Z. Wu, J. Yu, and S. Yuan, Strain-tunable magnetic and electronic properties of monolayer CrI_3, Phys. Chem. Chem. Phys. **21**, 7750 (2019).

[60] K. Riedl, D. Guterding, H. O. Jeschke, M. J. P. Gingras, and R. Valentí, *Ab initio* determination of spin Hamiltonians with anisotropic exchange interactions: The case of the pyrochlore ferromagnet $Lu_2V_2O_7$, Phys. Rev. B **94**, 014410 (2016).

[61] M. Mena, R. S. Perry, T. G. Perring, M. D. Le, S. Guerrero, M. Storni, D. T. Adroja, Ch. Rüegg, and D. F. McMorrow, Spin-wave spectrum of the quantum ferromagnet on the pyrochlore lattice $Lu_2V_2O_7$, Phys. Rev. Lett. **113**, 047202 (2014).

[62] Z. Liu, J.-W. Mei, and F. Liu, First-principles study of the organometallic $S = \frac{1}{2}$ kagome compound Cu(1,3-bdc), Phys. Rev. B **92**, 165101 (2015).

[63] S. Son, M. J. Coak, N. Lee, J. Kim, T. Y. Kim, H. Hamidov, H. Cho, C. Liu, D. M. Jarvis, P. A. C. Brown, J. H. Kim, C.-H. Park, D. I. Khomskii, S. S. Saxena, and J.-G. Park, Bulk properties of the van der Waals hard ferromagnet VI_3, Phys. Rev. B **99**, 041402(R) (2019).

[64] H. Lane, E. Pachoud, J. A. Rodriguez-Rivera, M. Songvilay, G. Xu, P. M. Gehring, J. P. Attfield, R. A. Ewings, and C. Stock, Two-dimensional ferromagnetic spin-orbital excitations in honeycomb VI_3, Phys. Rev. B **104**, L020411 (2021).

[65] L. D. Casto, A. J. Clune, M. O. Yokosuk, J. L. Musfeldt, T. J. Williams, H. L. Zhuang, M.-W. Lin, K. Xiao, R. G. Hennig, B. C. Sales, J.-Q. Yan, and D. Mandrus, Strong spin-lattice coupling in $CrSiTe_3$, APL Mater. **3**, 041515 (2015).

[66] Y. F. Li, W. Wang, W. Guo, C. Y. Gu, H. Y. Sun, L. He, J. Zhou, Z. B. Gu, Y. F. Nie, and X. Q. Pan, Electronic structure of ferromagnetic semiconductor $CrGeTe_3$ by angle-resolved photoemission spectroscopy, Phys. Rev. B **98**, 125127 (2018).

[67] A. Cvitkovic, N. Ocelic, and R. Hillenbrand, Analytical model for quantitative prediction of material contrasts in scattering-type near-field optical microscopy, Opt. Express **15**, 8550 (2007).

[68] A. J. L. Adam, Review of near-field terahertz measurement methods and their applications, J. Infr. Millimeter Terahertz Waves **32**, 976 (2011).

[69] X. Chen, D. Hu, R. Mescall, G. You, D. N. Basov, Q. Dai, and M. Liu, Modern scattering-type scanning near-field optical microscopy for advanced material research, Adv. Mater. **31**, 1804774 (2019).

[70] M. M. Wiecha, A. Soltani, and H. G. Roskos, *Terahertz Nano-Imaging with s-SNOM* (IntechOpen, London, 2021).

[71] R. S. Fishman, J. S. Gardner, and S. Okamoto, Orbital angular momentum of magnons in collinear magnets, Phys. Rev. Lett. **129**, 167202 (2022).

[72] G. Go, D. An, H.-W. Lee, and S. K. Kim, Magnon orbital nernst effect in honeycomb antiferromagnets without spin-orbit coupling, Nano. Lett. (2024), doi: 10.1021/acs.nanolett.4c00430.

[73] M. Lein and K. Sato, Krein-Schrödinger formalism of bosonic Bogoliubov–de Gennes and certain classical systems and their topological classification, Phys. Rev. B **100**, 075414 (2019).

[74] J. H. P. Colpa, Diagonalization of the quadratic boson Hamiltonian, Physica A **93**, 327 (1978).

[75] V. Cherepanov, I. Kolokolov, and V. L'vov, The saga of YIG: Spectra, thermodynamics, interaction and relaxation of magnons in a complex magnet, Phys. Rep. **229**, 81 (1993).

[76] S. Weinberg, *The Quantum Theory of Fields: Foundations* (Cambridge University Press, Cambridge, 1995), Vol. 1.

[77] J. Habel, A. Mook, J. Willsher, and J. Knolle, Breakdown of chiral edge modes in topological magnon insulators, Phys. Rev. B **109**, 024441 (2024).

[78] G. D. Mahan, *Many-Particle Physics* (Springer, Boston, 2000).

[79] A. Gurevich and G. Melkov, *Magnetization Oscillations and Waves* (Taylor & Francis, Milton Park, London, 1996).

[80] Y. O. Kvashnin, A. Bergman, A. I. Lichtenstein, and M. I. Katsnelson, Relativistic exchange interactions in CrX_3 (X = Cl, Br, I) monolayers, Phys. Rev. B **102**, 115162 (2020).

[81] B. Huang, G. Clark, E. Navarro-Moratalla, D. R. Klein, R. Cheng, K. L. Seyler, D. Zhong, E. Schmidgall, M. A. McGuire, D. H. Cobden, W. Yao, D. Xiao, P. Jarillo-Herrero, and X. Xu, Layer-dependent ferromagnetism in a van der Waals crystal down to the monolayer limit, Nature (London) **546**, 270 (2017).

[82] M. A. McGuire, H. Dixit, V. R. Cooper, and B. C. Sales, Coupling of crystal structure and magnetism in the layered, ferromagnetic insulator CrI_3, Chem. Mater. **27**, 612 (2015).

[83] E. Ruff, S. Widmann, P. Lunkenheimer, V. Tsurkan, S. Bordács, I. Kézsmárki, and A. Loidl, Multiferroicity and skyrmions carrying electric polarization in GaV_4S_8, Sci. Adv. **1**, e1500916 (2015).

[84] T. Kimura, T. Goto, H. Shintani, K. Ishizaka, T. Arima, and Y. Tokura, Magnetic control of ferroelectric polarization, Nature (London) **426**, 55 (2003).

[85] M. Kenzelmann, A. B. Harris, S. Jonas, C. Broholm, J. Schefer, S. B. Kim, C. L. Zhang, S.-W. Cheong, O. P. Vajk, and J. W. Lynn, Magnetic inversion symmetry breaking and ferroelectricity in $TbMnO_3$, Phys. Rev. Lett. **95**, 087206 (2005).

[86] J. Chaloupka, G. Jackeli, and G. Khaliullin, Kitaev-Heisenberg model on a honeycomb lattice: Possible exotic phases in iridium oxides A_2IrO_3, Phys. Rev. Lett. **105**, 027204 (2010).

[87] J. G. Rau, E. K.-H. Lee, and H.-Y. Kee, Generic spin model for the honeycomb iridates beyond the Kitaev limit, Phys. Rev. Lett. **112**, 077204 (2014).

[88] V. M. Katukuri, S. Nishimoto, V. Yushankhai, A. Stoyanova, H. Kandpal, S. Choi, R. Coldea, I. Rousochatzakis, L. Hozoi, and J. van den Brink, Kitaev interactions between j = 1/2 moments in honeycomb Na_2IrO_3 are large and ferromagnetic: Insights from *ab initio* quantum chemistry calculations, New J. Phys. **16**, 013056 (2014).

[89] E. Aguilera, R. Jaeschke-Ubiergo, N. Vidal-Silva, L. E. F. F. Torres, and A. S. Nunez, Topological magnonics in the two-dimensional van der Waals magnet CrI_3, Phys. Rev. B **102**, 024409 (2020).

[90] A. Kitaev, Anyons in an exactly solved model and beyond, Ann. Phys. **321**, 2 (2006).

[91] P. A. McClarty, X.-Y. Dong, M. Gohlke, J. G. Rau, F. Pollmann, R. Moessner, and K. Penc, Topological magnons in Kitaev magnets at high fields, Phys. Rev. B **98**, 060404(R) (2018).

[92] A. Mook, S. A. Díaz, J. Klinovaja, and D. Loss, Chiral hinge magnons in second-order topological magnon insulators, Phys. Rev. B **104**, 024406 (2021).